Revision 1

Crystal chemistry of schreibersite, $(Fe,Ni)_3P$

Sergey N. Britvin[1,2]*, Maria G. Krzhizhanovskaya[1], Andrey A. Zolotarev[1], Liudmila A. Gorelova[1], Edita V. Obolonskaya[3], Natalia S. Vlasenko[4], Vladimir V. Shilovskikh[4,5] and Mikhail N. Murashko[1]

[1]Institute of Earh Sciences, St. Petersburg State University, Universitetskaya Nab. 7/9, 199034 St. Petersburg, Russia

[2]Kola Science Center, Russian Academy of Sciences, Fersman Str. 14, 184209 Apatity, Russia

[3]The Mining Museum, Saint Petersburg Mining University, 2, 21st Line, 199106 St. Petersburg, Russia

[4]Centre for Geo-Environmental Research and Modelling, St. Petersburg State University, Ulyanovskaya ul. 1, 198504 St. Petersburg, Russia

[5]Institute of Mineralogy, Urals Branch of Russian Academy of Science, Miass 456317, Russia

Abstract

Schreibersite, $(Fe,Ni)_3P$, the most abundant cosmic phosphide, is a principal carrier of phosphorus in the natural Fe–Ni–P system and a likely precursor for prebiotic organophosphorus compounds at the early stages of Earth's evolution. The crystal structure of the mineral bears three metal sites allowing for unrestricted substitution of Fe for Ni. The distribution of these elements across the structure could serve as a tracer of crystallization conditions of schreibersite and its parent celestial bodies. However, discrimination between Fe ($Z = 26$) and Ni ($Z = 28$) based on the conventional X-ray structural analysis was for a long time hampered due to the proximity of their atomic scattering factors. We herein show that this problem has been overcome with the implementation of area detectors in the practice of X-ray diffraction. In this paper we report on previously unknown site-specific substitution trends in schreibersite structure. The composition of the studied mineral encompasses a Ni content ranging between 0.03 and 1.54 Ni atoms per formula unit (*apfu*): the entire Fe-dominant side of the join Fe_3P–Ni_3P. Of 23 schreibersite crystals studied, 22 comprise magmatic and non-magmatic iron meteorites and main group pallasites. The near end-member mineral (0.03 Ni *apfu*) comes from the pyrometamorphic rocks of the Hatrurim Basin, Negev desert, Israel. It was found that Fe/Ni substitution in schreibersite follows the same trends in all studied meteorites. The dependencies are non-linear and can be described by 2nd order polynomials. However, substitution across the *M*2 and *M*3 sites within the most common range of compositions ($0.6 < Ni < 1.5$ *apfu*) is well approximated by a linear regression: $Ni(M2) = 0.84 \times Ni(M3) - 0.30$ *apfu* (standard error 0.04 Ni *apfu*). The analysis of the obtained results shows a strong divergence between the behavior of unit-cell parameters of natural schreibersite and those of synthetic $(Fe,Ni)_3P$. This indicates that Fe/Ni substitution trends in the mineral and its synthetic surrogates are different. A plausible explanation might be related to the differences in the system equilibration time of meteoritic schreibersite (millions of years) and synthetic $(Fe,Ni)_3P$ (~100 days). However, regardless of the reason for the observed difference, synthetic $(Fe,Ni)_3P$ can not be considered a

structural analogue of natural schreibersite, and this has to be taken into account when using synthetic $(Fe,Ni)_3P$ as an imitator of schreibersite in reconstructions of natural processes.

Keywords: phosphide; schreibersite; Fe_3P, Fe–Ni–P system; meteorite; planetary interiors; crystal structure; solid solution

Introduction

Schreibersite, $(Fe,Ni)_3P$ (Berzelius 1832) is the most common natural phosphide and a general carrier for reduced phosphorus in meteoritic matter (Doan and Goldstein 1969). The mineral may constitute for up to 14 % of metal matrix in iron and stony-iron meteorites (Buchwald 1975; Wasson and Choe 2009). Being a dominant phosphide phase in the metal-rich part of the Fe–Ni–P(S) system, schreibersite is a regular subject of studies devoted to evolution of planetary interiors (e.g., Clarke and Goldstein 1978; Scott et al. 2007; Goldstein et al. 2009; Gu et al. 2014, 2016; He et al. 2019; Khisina et al. 2019; Chabot et al. 2020; Chornkrathok et al. 2020). The mineral is a typical constituent of enstatite chondrites and achondrites (Wasson and Wai 1970); it was encountered in carbonaceous chondrites (Zolensky et al. 2002), acapulcoites, lodranites and winonaites (Li et al. 2011; Keil and McCoy 2018) and in Lunar rocks (Smith and Steele 1976; Gleißner and Becker 2017). Thermodynamic calculations evidence that schreibersite could be a primary phosphorus-bearing phase formed during solar nebula condensation (Pasek 2008). The mineral is considered a likely source of low-valent phosphorus which was required for initiation of prebiotic phosphorylation processes on early Earth (e.g., Bryant et al. 2013; Pasek 2020).

Investigation of synthetic compounds has showed that phosphides Fe_3P and Ni_3P are isostructural and form a continuous series of solid solutions (Rundqvist 1962; Rundqvist et al. 1962; Spriggs 1970). The composition of rarely occurring terrestrial schreibersite approaches pure Fe_3P (e.g., Britvin et al. 2017b). On the contrary, meteoritic mineral is always enriched in Ni, forming a tie-line towards the Ni-dominant counterpart, nickelphosphide $(Ni,Fe)_3P$ (Britvin et. al. 1999). In spite of a simple composition, schreibersite has a complex crystal structure which contains one 9-coordinated phosphorus site and three cage-like metal-centered polyhedra: *M*1 (coordination number 15), *M*2 (14) and *M*3 (13) (Figure 1). The polyhedra, which have no analogues among other Fe-Ni phosphides (Britvin et al. 2020a), are arranged into the three-dimensional framework. The reliable determination of Fe/Ni distribution across the metal sites was the main challenge of schreibersite

crystal chemistry. Doenitz (1970) has demonstrated on the mineral from the North Chile (Tocopilla) meteorite that Ni in schreibersite preferably occupies *M*3 and *M*2 structural sites in the ratio of ~2/1, avoiding *M*1 site. This finding might have promising implications, as distribution of Fe and Ni across the different sites of schreibersite structure could be related to crystallization pathways of metal-rich meteorites and their parent bodies. A serious obstacle towards exploring this hypothesis was a proximity of X-ray scattering factors of Fe ($Z = 26$) and Ni ($Z = 28$), that makes quantitative X-ray refinement of Fe/Ni populations a difficult task (e.g., Hawthorne 1983; Warner et al. 1995). Because of that, Doenitz (1970) and the successors (Moretzki et al. 2005) have used various techniques based on the effect of anomalous scattering of X-rays at the Fe-*K* absorption edge. However, the experimental limitations allowed only semi-quantitative estimation of Fe/Ni site populations and restricted the number of studied crystals to a few samples.

In the course of an ongoing research of natural phosphides, we have found that Fe/Ni population across the metal sites of schreibersite structure can be determined with high precision using a conventional X-ray structural analysis, due to implementation of high-redundancy and high-intensity datasets obtained using area-detector diffractometers. The results reported herein represent the crystal chemistry of the entire Fe-dominant side of natural solid solutions Fe_3P–Ni_3P.

Materials and Methods

Schreibersite

Meteorite samples (Table 1) were kindly provided by the Mining Museum, Saint Petersburg Mining University, except for a slice of the Mont Dieu octahedrite which was courteously donated by Dr. Alain Carion (carionmineraux.com). Schreibersite grains were either hand-picked from polished sections using a tungsten carbide needle or extracted from meteorite chips by the dissolution of metal matrix in a diluted HCl.

98 **Electron microprobe analysis (EMPA)**

99 EMPA was performed from polished sections coated with a carbon film. Fe, Ni and P
100 contents were determined by means of a Hitachi S-3400N SEM equipped with an Oxford
101 Instruments AzTec Energy X-Max 20 EDX spectrometer (20 kV, 1 nA). Cobalt content was
102 determined with an INCA WAVE 500 WDX spectrometer (20 kV, 15 nA). Schreibersite of known
103 composition and Co metal were used as analytical standards. Neither silicon nor sulfur was detected
104 in the mineral. No compositional zoning was observed. The complete EMPA results are provided in
105 Supplemental Tables S1 and S2.
106
107 **X-ray single-crystal study**
108 The datasets were collected by means of two instruments, Bruker Smart APEXII CCD
109 (conventional sealed tube) and Bruker Kappa APEX DUO (kappa-geometry, microfocus mirror
110 optics). Both devices were equipped with the identical 1024K APEXII CCD detectors and were
111 operated using Mo*K*α-radiation. The choice of the instrument was determined by the crystal size and
112 the time available for current measurement. For each crystal, a full Ewald sphere up to $2\Theta = 64°$
113 ($\sin\Theta/\lambda = 0.746$ Å^{-1}) was scanned with a frame width of 1°. The collection times were adjusted to
114 attain the average $I/\sigma(I)$ ratio not less than 30. Data processing and integration included standard
115 routines incorporated into a Bruker APEX2 software. In order to avoid the problem of low accuracy
116 of unit-cell measurements with area detectors (Duisenberg et al. 2000), we used the unit-cell
117 parameters refined from the Rietveld data (see below). The absorption correction was performed
118 with a SADABS multi-scan procedure (Sheldrick 2015a). The HKL files were generated unmerged
119 in HKLF4 format. Crystal structures were solved by an intrinsic phasing method as implemented in
120 *SHELXT*-2018, using Olex2 operational environment (Sheldrick 2015b; Dolomanov et al. 2009).
121 Because schreibersite crystallizes in a non-centrosymmetric space group $I\bar{4}$ (# 82), atomic
122 coordinates (but not HKL source files) were transformed when necessary to either standard (Doenitz

1970) or inverse setting. Structure refinements were carried out using full-matrix least-square approach with a *SHELXL*-2018 software (Sheldrick 2015a). All sites in the crystal structure were treated as fully occupied, based on the results of EMPA and previous reports on schreibersite stoichiometry. Metal sites were first checked for mixed Fe/Ni population using standard *SHELXL* procedures. In case when population of a site by a minor substituent (either Fe or Ni) exceeded 3σ (*apfu*), the site was refined as having mixed Fe/Ni occupancy. Otherwise, site population was fixed to 1 (Fe or Ni, respectively). A brief summary of data collection and refinement parameters prepared using a *publCIF* software (Westrip 2010) is given in Supplemental Table S3. Full details can be retrieved from crystallographic information file (CIF) included in Supplemental Materials.

Rietveld refinements.

Powder X-ray diffraction patterns were recorded from the same crystal fragments which were used for the single-crystal study. A Rigaku RAXIS Rapid II diffractometer (semi-cylindrical imaging plate, Debye-Scherrer geometry, r = 127.4 mm) was equipped with a rotating anode Co$K\alpha$-radiation source (40 kV, 15 mA) and microfocus X-ray optics. The imaging plate was calibrated with a NIST silicon standard. Powdered schreibersite was mixed with an epoxy resin into the balls of 0.15-0.2 mm in diameter. The balls were pinned onto the glass fibers and exposed to X-rays for 30 min with a simultaneous φ-axis rotation. The imaging plate-to-profile conversion was performed by use of an osc2xrd program (Britvin et al. 2017a). Full-profile Rietveld refinements were carried out using a Bruker TOPAS v.5.0 software (Coelho 2018). The two-stage refinement procedure was employed. At first, the unit-cell parameters alone were refined by Rietveld method using the input data (including site occupancies) taken from the initial single-crystal refinements. These refined unit-cell parameters (Table 2) were used in final refinements of all single-crystal datasets. At the second stage, the powder diffraction patterns were re-refined by Rietveld method based on the input atomic coordinates, site occupancies and displacement parameters acquired from final single-crystal

data. During this, last Rietveld refinement stage, all parameters were freely refined, except for the displacement values of the metal sites which were treated as being linked via the same B_{eq} (based on the nearly the same U_{iso} obtained in the single-crystal datasets). The only sample where we did not refine atomic coordinates was the Fe_3P end-member from Hatrurim (Htr). The full-profile refinement allowed to achieve a precision of 5×10^{-4} Å for the *a* parameter and 3×10^{-4} Å for the *c* parameter, as it was confirmed by comparison of imaging plate data with the Si-calibrated test profile of GM sample obtained using a Bruker Phaser II diffractometer (Bragg-Brentano geometry). Data collection and Rietveld refinement details are summarized in Supplemental Table S4. The snapshots of refinement plots can be viewed in Supplemental Figures S4-S26. Further details of the Rietveld refinements, including observed, calculated and background profile listings, can be retrieved from the powder CIF files included into Supplemental Materials.

Results

Occurrence and chemical composition

Of 23 schreibersite crystals subjected to this study (Table 1), 22 originate from 13 iron meteorites belonging to magmatic and non-magmatic groups (e.g., Goldstein et al. 2009) and 6 main-group pallasites (e.g., Boesenberg et al. 2012). The terrestrial mineral (Figure 2) comes from the pyrometamorphic rocks of the Halamish Wadi, Hatrurim Basin, Israel (e.g., Britvin et al. 2015). Meteoritic schreibersite is represented by 0.1–0.5 mm single-crystal fragments extracted from the α-(Fe,Ni) (kamacite) matrix, except for the sample Crn2 (Cranbourne) comprised of so-called "rhabdite" (schreibersite variety having needle-like habit). The Ni-depleted schreibersite from Zacatecas (1792) (Table 1) represents the rim surrounding the troilite nodule. The grain morphology of the mineral from the listed meteorites (except for Mont Dieu) was described by Buchwald (1975) and Buseck (1977). Terrestrial schreibersite is of interest due to its association: the mineral is being

172 replaced by the polycrystalline rims of barringerite, Fe_2P (Figure 2), exactly in the same manner as it
173 has been reported in meteoritic assemblages (Buseck 1969; Britvin et al. 2020b).

174 Nickel contents in the studied mineral cover a range from 0.03 to 1.54 *apfu* (Table 1) and
175 thus encompass the entire schreibersite half (Fe > Ni) of the join Fe_3P–Ni_3P. All analyses
176 correspond to a stoichiometry of M_3P (Supplemental Table S2), indicating for the absence of
177 partially vacant sites in the crystal structure, in agreement with the previously reported data. One of
178 the aims of the present work was an investigation of Fe for Ni substitution that required X-ray
179 refinement of site populations. The precision of conducted X-ray refinements can be estimated via
180 comparison of total Ni contents determined by electron microprobe and those derived from the X-
181 ray structural analysis (Table 1, Figure 3). It can be seen that the sums of Ni site populations
182 obtained from single-crystal and Rietveld refinements quantitatively match the results of EMPA
183 within the standard errors of 0.04 and 0.01 Ni *apfu*, respectively (Figure 3).

184

185 **Absolute structure**

186 Schreibersite crystallizes in a non-centrosymmetric space group $I\bar{4}$ that implies the existence
187 of two spatial atomic arrangements called *absolute structures*. These arrangements, being related by
188 an inversion operator, are designated as a *standard* absolute structure and an *inverse* one. The
189 assignment of a crystal to a certain absolute structure can be done based on the differences in the
190 intensities of Friedel reflection pairs, using a measure known as an absolute structure (Flack *x*)
191 parameter (Flack and Bernardinelli 1999). The latter can vary between 0 (standard setting) and 1
192 (inverse one); the intermediate values indicate the occurrence of inversion (racemic) twinning. The
193 possibility of absolute structure determination for any given pair of X-ray wavelength/crystal
194 composition can be evaluated using a *Friedif* coefficient (Flack and Shmueli 2007). The chemical
195 composition of schreibersite (*Friedif* > 200) allows convincing determination of absolute structure
196 using Mo*K*α-radiation. Of 23 schreibersite crystals studied herein, 13 were found to adopt standard

197 setting relative to that of Doenitz (1970), 7 have inverse absolute structure, and 3 represent inversion
198 twins (Table 2). These results show significant predominance of the crystals having standard
199 absolute structure, in contrast to the results by Skála and Císařová (2005) who reported the
200 prevalence of inverse setting (6) among 8 schreibersite crystals from 5 iron meteorites. The overall
201 count of schreibersite having the confirmed standard setting (including the crystal reported by
202 Doenitz (1970) is 16 crystals. 13 crystals have an inverse absolute structure, and in 3 cases the
203 mineral exhibits significant degree of racemic twinning. Therefore, based on the known data, one
204 can not postulate the predominance of either absolute structure among natural schreibersite.
205
206 **Unit-cell parameters of schreibersite and synthetic analogues**
207 The unit-cell parameters of studied crystals are listed in Table 2 and plotted in Figure 4.
208 Several authors reported lattice parameters of natural schreibersite (e.g., Skála and Císařová 2005;
209 Geist et al. 2005; He et al. 2019 and the references cited therein). However, all published results
210 were obtained with the use of single-crystal diffractometers whose precision corresponds to the 3rd
211 decimal place, whereas the 4th digit reflects the tightness of least-squares convergence. Besides, not
212 all papers provide electron microprobe data for the mineral. This has led to disparate results well
213 illustrated by the diffuse character of *a*/*c* ratio scatter plots (e.g., Geist et al. 2005). The
214 discrepancies between chemical composition and unit-cell metrics of schreibersite were also
215 discussed by Skála and Císařová (2005). Because of apparent heterogeneity of the published single-
216 crystal data, we herein compare only those reference parameters which were refined by the whole-
217 pattern profile fitting and thus have a precision of the 4rd decimal place. All these results belong to
218 the synthetic solid solutions Fe_3P–Ni_3P (Skála and Drábek 2000; 2003).
219 The *a* parameter of natural schreibersite and its synthetic analogues follows the same trend
220 (Figure 4a). However, consolidation of the present results with the data by Skála and Drábek (2000;
221 2003) demonstrates that this dependence is not linear as it was suggested previously but obeys very

222 flat 2nd order polynomial regression. The latter gives an intercept of 9.1084(12) Å, coincident with
223 the *a* parameter of 9.1085(3) Å experimentally determined for pure Fe_3P (Skála and Drábek 2000).
224 The dependence of unit-cell volume (Figure 4b) also complies with the 2nd order polynomial as it
225 was noticed by Spriggs (1970) and discussed by Skála and Drábek (2000). The intercept of the
226 volume/composition fit, 370.3(2) $Å^3$, coincides with the experimental value of 370.22(2) $Å^3$ for Fe_3P
227 (Skála and Drábek 2000). In contrast to the *a* parameter and cell volume, the behaviour of the *c*
228 parameter of natural schreibersite is completely distinct from that of its synthetic analogues (Figure
229 4c). The latter were shown to obey the 2nd order polynomial regression (Spriggs 1970; Skála and
230 Drábek 2000). On the contrary, our data clearly demonstrate that the *c* parameter of natural mineral
231 follows quasi-linear dependence up to the Ni-richest composition (1.54 Ni *apfu*). The observed
232 divergence is emphasized further by plotting the *c*/*a* parameter ratios (Figure 4d). These values are
233 nearly the same for the Fe_3P and Ni_3P end-members, and because of that, *c*/*a* ratio is a very sensitive
234 indicator of any cell distortions, though requires high-precision data. The consequences rising from
235 the observed differences are discussed below.
236
237 **Site populations**
238 A quantitative match between Ni contents determined by EMPA and the values obtained
239 from the X-ray single-crystal data evidences that the uncertainties in the values of Ni population
240 (Table 3) represent the real precision of the refinements. The precision of the Rietveld data in Table
241 3 can be overestimated, as it is typical for the Rietveld refinement results. Nevertheless, cross-
242 plotting of site populations determined by the two methods (Figure 5) ensures the data consistency.
243 Single-crystal refinements of the *M*1 site did not reveal Ni occupancy factors exceeding 3σ
244 *apfu*, confirming the previous observations that Ni avoids incorporation in this position (e.g.,
245 Doenitz 1970). The formerly obscured substitution trends for the *M*2 and *M*3 sites are illustrated by
246 Figure 6a. Both sites exhibit non-linear dependencies of Ni incorporation upon the linear increase of

247 total Ni content. The *M*3 trend demonstrates significant offset from the theoretical tie-line Fe_3P–
248 Ni_3P. In spite of the general nonlinearity, Fe for Ni substitution across the wide range of
249 compositions, from 0.6 to 1.5 total Ni *apfu*, can be well approximated by two virtually parallel linear
250 trends separated by statistically significant difference (Figure 6b). The overall interdependence can
251 be expressed by linear equation:

252 $$\mathrm{Ni}(M2) = 0.84 \times \mathrm{Ni}(M3) - 0.30 \textit{ apfu} \; [R^2 = 0.91, \text{standard error } 0.04 \text{ Ni } \textit{apfu}] \qquad (1)$$

253 The equality of both regression slopes to the value of 1/2 (Figure 6b) evidences that incorporation of
254 Ni across this range proceeds through a highly ordered pathway, most probably – through a coupled
255 substitution of 2Fe for 2Ni, according to a scheme: $\mathrm{Fe}(M2) + \mathrm{Fe}(M3) \rightarrow \mathrm{Ni}(M2) + \mathrm{Ni}(M3)$.

256 The important consequence raised from equation (1) is that the *M*3 site in natural
257 schreibersite attains full Ni saturation (Ni3 = 1 *apfu*) exactly at the borderline with nickelphosphide
258 (total Ni = 1.5 *apfu*) (Figure 6a). The significant departures of both substitution trends from the
259 straight tie-line Fe_3P–Ni_3P (Figure 6a) explain the observed violations of lattice parameters from
260 Vegard's law (e.g., Zen 1956) (*cf.* Figure 4). The dependencies of *c*/*a* parameter ratio on Ni site
261 population are illustrated in Figure 7. The influence of Ni population at the *M*3 site can be described
262 by a linear regression, whereas substitution at the *M*2 site follows 2nd order polynomial.
263 Consequently, the quasi-linear dependence of *c*/*a* ratio on the chemical composition (Figure 4d)
264 represent superposition of two regressions plotted in Figure 7, with predominant influence of
265 substitution at the *M*3 site.

266

267 **Interatomic bonds**

268 The complex shape of coordination polyhedra in schreibersite (Figure 1) determines the large
269 number of interatomic interactions, whereas the metallic type of bonding (La Cruz et al. 2016) and
270 high metal/phosphorus ratio implies the occurrence of both intermetallic and metal-phosphorus
271 interactions. Of 26 symmetrically independent bonds in the schreibersite structure, 9 comprise the

272 *M*–P linkages within the phosphorus-centered polyhedron [PM_9] (Figure 1a). The remaining 17
273 metal-metal bonds maintain the integrity of non-convex metal-centered polyhedra (Figure 1b-d).
274 The lengths of *M*–P bonds spread within a narrow range of values, between 2.23–2.35 Å. In
275 contrast, the lengths of intermetallic bonds vary considerably from 2.41 (*M*1–*M*1) to 3.02 Å (*M*2–
276 *M*2). The high precision of conducted experiments and ability to discriminate between Fe and Ni
277 allowed plotting the site-specific dependencies for every bond (Supplementary Figure S1–S3).
278 However, the revealed trends were found to be rather complex and have no simple relations to
279 crystallographic directions in the structure. Therefore, we herein restrict the comments to a few of
280 the most representative examples. The intermetallic linkage *M*2–*M*2^{ix} is being most sensitive to Ni
281 incorporation, both in the *M*2 and *M*3 site (Figure 8a). Although both sites show steep negative
282 trends of bond length upon increase of Ni content, these dependencies are described by two
283 completely different curves. Another intermetallic bond, *M*3–*M*3^{vii}, exhibits the maximal steepness
284 of bond-length ramp with an increasing Ni site population (Figure 8b). However, contrary to the first
285 example, the variations in bond length are very flat and thus much less sensitive to changes in the
286 chemical composition. The "knee-fold" shapes of *M*1–*M*3^{ii} trends (Figure 8c) indicate for some yet
287 obscured interatomic interactions which abruptly turn the observed substitution dependencies. The
288 *M*2–P bond is quite interesting because of almost complete insensitivity to Fe for Ni substitution
289 (Figure 8d). The overall change in the *M*2–P bond length is 0.004 Å. The indifference of *M*2–P bond
290 to compositional changes might make it useful in practice, e.g. in revealing the obvious outliers in
291 the bond length which would worth of additional investigation.
292

293 **Discussion**

294 **Refinement of similar X-ray scatterers: a Fe/Ni case**

295 In spite of a progress in X-ray diffraction techniques, the proper determination of similar X-
296 ray scatterers in solid solutions remains a challenge of mineralogical crystallography (Hawthorne

297 1983; Angel and Nestola 2016). The case of Fe (Z = 26) and Ni (Z = 28) is an example of the
298 element pair whose difference in (non-anomalous) scattering power is considered insufficient for the
299 site population refinement (e.g., Warner et al. 1995; Moretzki et al. 2005). We herein provided the
300 statistically proven evidence that X-ray single-crystal refinement using MoKα-radiation can be
301 regarded a quantitative method for discrimination between similar scatterers such as Fe and Ni
302 (Figure 3, 5-8). This result might look somewhat unexpected, in view of not using the effect of
303 anomalous dispersion at the Fe-K absorption edge (e.g., Doenitz et al. 1970; Moretzki et al. 2005).
304 However, a calculation of the difference between scattering factors of Fe and Ni gives a value of
305 7.3% for MoKα-radiation (Supplementary Table S5). This value is twice smaller than the difference
306 attainable using anomalous scattering with CoKα (15.4%), but it is not small. As for comparison, it
307 was shown that the good quality X-ray data allow determination of very subtle (down to 0.4 %)
308 differences between the intensities of Friedel opposites (e.g., Flack and Shmueli 2007). The X-ray-
309 based refinement of similar scatterers has become possible with the implementation of area detectors
310 in practice of X-ray diffraction. The problems of redundancy, intensity, resolution, treatment of
311 absorption and extinction were the factors critically limiting the reliability of site occupancy analysis
312 with the data collected using point-counting detectors (e.g., Kroll et al. 1997). All these problems
313 are nowadays diminished to a degree of routine procedures due to usage of area detectors. The
314 detailed discussion of experimental conditions required for reliable discrimination between similar
315 X-ray scatterers lies beyond the scope of the present paper. However, the main conditions can be
316 formulated as: (1) High-redundancy datasets (full Ewald sphere is preferable), (2) High-brightness
317 data (average $I/\sigma(I)$ ratio between 30 and 100), (3) Data-to-parameter ratio not less than 8 (a
318 standard CheckCIF requirenment).
319
320
321

322 **Fe/Ni substitution trends: natural schreibersite *vs* synthetic $(Fe,Ni)_3P$**

323 The important consequence rising from the present work is that the trends in ordered Fe/Ni
324 substitution are the same for schreibersite originated from different meteorite groups, i.e., from
325 magmatic and non-magmatic irons and pallasites. This evidences for the similarity of schreibersite
326 crystallization conditions, most probable – for the time required for intersite equilibration between
327 Fe and Ni.

328 The precise refinements of unit-cell parameters and site populations have showed that the *c*
329 parameter and *c*/*a* ratio of schreibersite are sensitive indicators of site-specific ordering of Fe and Ni
330 (Figure 4cd, 7). Although both natural mineral and its synthetic counterparts exhibit substantial
331 violations from Vegard's law, there is an apparent difference in their parameters' behaviour. The
332 abrupt divergence in the *c*/*a* ratio trends (Figure 4d) evidences that Fe for Ni substitution in natural
333 schreibersite proceeds through a pathway different from that of synthetic $(Fe,Ni)_3P$. Therefore, one
334 can conclude that natural schreibersite is not structurally identical to synthetic $(Fe,Ni)_3P$ having the
335 same bulk composition. The latter does not depend on the route used for the synthesis of $(Fe,Ni)_3P$:
336 Spriggs (1970) investigated the fused Fe_3P–Ni_3P samples whereas Skála and Drábek (2000; 2003)
337 studied the sintered ones, and both authors demonstrate the similar trends in variations of unit-cell
338 parameters. Unfortunately, the absence of site-specific Fe/Ni distribution data for synthetic
339 $(Fe,Ni)_3P$ precludes further comparison with the results reported in the present work. However, one
340 can speculate that the observed differences may relate to the Fe/Ni ordering schemes, which in turn
341 can be dependent on different system equilibration times of meteoritic schreibersite (millions of
342 years, e.g., Goldstein et al. 2009) and synthetic $(Fe,Ni)_3P$ (up to 110 days, Skála and Drábek 2000).
343 The discrepancy between meteoritic schreibersite and synthetic $(Fe,Ni)_3P$ may be important in view
344 of a wide usage of schreibersite surrogates as simulants of natural mineral (Pasek et al. 2007; Pech
345 et al. 2011; Pirim et al. 2014; La Cruz et al. 2016; Parker et al. 2016). It was shown previously that
346 the crystal structures of phosphides substantially affect their surface chemistry and hence – the

pathways of surface reactions (e.g., Wexler et al. 2017; Li et al. 2019). The latter should not be ignored in the experiments aimed at mimicking the natural processes, such as biomimetic phosphorylation reactions. Besides, structural differences may considerably affect the behaviour of studied phases in the high-pressure/high-temperature experiments imitating the conditions characteristic of planetary interiors.

Implications

The results disclosed in the present work might have both fundamental and applied consequences. The knowledge of structural and compositional trends in the dominant cosmic phosphide may serve a basement for the further studies aimed at understanding crystallization histories of metal-rich interiors of celestial bodies. The obvious structural differences revealed between natural schreibersite and synthetic $(Fe,Ni)_3P$ may warn for the caution that should be undertaken while working with the synthetic schreibersite surrogates. The important applied result of this study is that we have showed the possibility of reliable X-ray refinements of structural sites occupied by similar X-ray scatterers, such as Fe and Ni.

Acknowledgments

The authors are grateful to curators of the Mining Museum, Saint Petersburg Mining University, and to Alain Carion for providing meteorite samples used in this work. We are thankful to Associate Editor Fabrizio Nestola for editorial handling of the manuscript. The referees, Roman Skála and Konstantin Litasov, are gratefully acknowledged for valuable comments and suggestions that helped the authors to improve the quality of the manuscript. This research is funded by Russian Science Foundation, grant 18-17-00079. The authors thank X-ray Diffraction Centre, "Geomodel" Resource Centre and Nanophotonics Resoure Centre of St. Petersburg State University for providing instrumental and computational resources.

372

373 **References cited**

374 Angel, R.J., and Nestola, F. (2016) A century of mineral structures: How well do we know them?
375 American Mineralogist, 101, 1036–1045.
376 Berzelius, J.J. (1832) Undersökning af en vid Bohumiliz I Böhmen funnen jernmassa. Kongelige
377 Svenska Vetenskaps-Academiens Handlingar, 106–119.
378 Boesenberg, J.S., Delaney, G.S., and Hewins, R.H.J. (2012) A petrological and chemical
379 reexamination of Main Group pallasite formation. Geochimica et Cosmochimica Acta, 89,
380 134–158.
381 Britvin, S.N., Dolivo-Dobrovolsky, D.V., and Krzhizhanovskaya, M.G. (2017a) Software for
382 processing the X-ray powder diffraction data obtained from the curved image plate detector of
383 Rigaku RAXIS Rapid II diffractometer. Zapiski Rossiiskogo Mineralogicheskogo
384 Obshchestva, 146, 104–107 (in Russian).
385 Britvin S.N., Murashko M.N., Vapnik E., Polekhovsky Y.S., Krivovichev S.V. (2017b) Barringerite
386 Fe_2P from pyrometamorphic rocks of the Hatrurim Formation, Israel. Geology of Ore
387 Deposits, 59, 619–625.
388 Britvin, S.N., Kolomensky, V.D., Boldyreva, M.M., Bogdanova, A.N., Kretser, Yu.L., Boldyreva,
389 O.N., and Rudashevskii, N.S. (1999) Nickelphosphide, $(Ni,Fe)_3P$, the nickel analog of
390 schreibersite. Zapiski Vsesoyuznogo Mineralogicheskogo Obshchestva, 128, 64–72 (in
391 Russian).
392 Britvin, S.N., Murashko, M.N., Vapnik, Ye., Polekhovsky, Yu.S., and Krivovichev, S.V. (2015)
393 Earth's phosphides in Levant and insights into the source of Archaean prebiotc phosphorus.
394 Scientific Reports, 5, 8355.

Britvin, S.N., Murashko, M.N. Vapnik, Ye., Polekhovsky, Yu.S., Krivovichev, S.V., Vereshchagin, O.S., Shilovskikh, V.V., and Krzhizhanovskaya, M.G. (2020a) Negevite, the pyrite-type NiP_2, a new terrestrial phosphide. American Mineralogist, 105, 422–427.

Britvin, S.N., Murashko, M.N., Vapnik, Ye., Polekhovsky, Yu.S., Krivovichev, S.V., Krzhizhanovskaya, M.G., Vereshchagin, O.S., Shilovskikh, V.V., and Vlasenko, N.S. (2020b) Transjordanite, Ni_2P, a new terrestrial and meteoritic phosphide, and natural solid solutions barringerite–transjordanite (hexagonal Fe_2P–Ni_2P). American Mineralogist, 105, 428–436.

Bryant, D.E., Greenfield, D., Walshaw, R.D., Johnson, B.R.G., Herschy, B., Smith, C., Pasek, M.A., Telford, R., Scowen, I., Munshi, T., Edwards, H.G.M., Cousins, C.R., Crawford, I.A., and Kee, T.P. (2013) Hydrothermal modification of the Sikhote-Alin iron meteorite under low pH geothermal environments. A plausibly prebiotic route to activated phosphorus on the early Earth. Geochimica et Cosmochimica Acta, 109, 90−112.

Buchwald, V.F. (1975) Handbook of iron meteorites. University of California Press, Berkeley, Los Angeles, London.

Buseck, P.R. (1969) Phosphide from meteorites: Barringerite, a new iron-nickel mineral. Science, 165, 169–171.

Buseck, P.R. (1977) Pallasite meteorites - mineralogy, petrology and geochemistry. Geochimica et Cosmochimica Acta, 41, 711–740.

Chabot, N.L., Cueva, R.H., Beck, A.W., and Ash, R.D. (2020) Experimental partitioning of trace elements into schreibersite with applications to IIG iron meteorites. Meteoritics & Planetary Science, doi: 10.1111/maps.13462.

Chornkrathok, S., Zhang, D., and Dera, P. (2020) Structure and behavior of the Ni end-member schreibersite Ni_3P under compression to 50 GPa. Minerals, 10, 306.

418 Clarke, R.S., and Goldstein, J. (1978) Schreibersite growth and its influence on the metallography of
419 coarse-structured iron meteorites, 83 p. Smithsonian Contributions to the Earth Sciences, no.
420 21. Smithsonian Institution Press, Washington, D.C.
421 Coelho, A.A. (2018) TOPAS and TOPAS − Academic: an optimization program integrating
422 computer algebra and crystallographic objects written in C++. Journal of Applied
423 Crystallography, 51, 210–218.
424 Doan A.S., Jr., and Goldstein, J.I. (1969). The formation of phosphides in iron meteorites. Meteorite
425 Research, 12, 763–779.
426 Doenitz, F.D. (1970) Die Kristallstruktur des meteoritischen Rhabdites $(Fe,Ni)_3P$. Zeitschrift für
427 Kristallographie, 131, 222–236.
428 Dolomanov, O.V., Bourhis, L.J., Gildea, R.J., Howard, J.A., and Puschmann, H. (2009) OLEX2: a
429 complete structure solution, refinement and analysis program. Journal of Applied
430 Crystallography, 42, 339–341.
431 Duisenberg, A.J.M., Hooft, R.W.W., Schreurs, A.M.M., and Kroon, J. (2000) Accurate cells from
432 area detector images. Journal of Applied Crystallography, 33, 893–898.
433 Flack, H.D., and Bernardinelli, G. (1999) Absolute structure and absolute configuration. Acta
434 Crystallographica, A55, 908–915.
435 Flack, H.D., and Shmueli, U. (2007) The mean-square Friedel intensity difference in *P*1 with a
436 centrosymmetric substructure. Acta Crystallographica, A63, 257–265.
437 Geist, V., Wagner, G., Nolze, G., and Moretzki, O. (2005) Investigations of the meteoritic mineral
438 $(Fe,Ni)_3P$. Crystal Research and Technology, 40, 52–64.
439 Gleißner, P., and Becker, H. (2017) Formation of Apollo 16 impactites and the composition of late
440 accreted material: constraints from Os isotopes, highly siderophile elements and sulfur
441 abundances. Geochimica et Cosmochimica Acta , 200, 1–24.

442 Goldstein, J.I., Scott, E.R.D., and Chabot, N.L. (2009). Iron meteorites: Crystallization, thermal
443 history, parent bodies, and origin. Chemie der Erde–Geochemistry, 69, 293–325.
444 Grady, M.M. (2000) Catalogue of meteorites, 5th edition. London, The Natural History Museum.
445 Gu, T., Fei, Y., Wu, X., and Qin, S. (2014) High-pressure behavior of Fe_3P and the role of
446 phosphorus in planetary cores. Earth and Planetary Science Letters, 390, 296–303.
447 Gu, T.; Fei, Y.; Wu, X.; and Qin, S. (2016) Phase stabilities and spin transitions of $Fe_3(S_{1-x}P_x)$ at
448 high pressure and its implications in meteorites. American Mineralogist, 101, 205–210.
449 Hawthorne, F.C. (1983) Quantitative characterization of site occupancies in minerals. American
450 Mineralogist, 68, 287–306.
451 He, X.J., Guo, J.Z., Wu, X., Huang, S.X., Qin, F., Gu, X.P., and Qin, S. (2019) Compressibility of
452 natural schreibersite up to 50 GPa. Physics and Chemistry of Minerals, 46, 91–99.
453 Keil, K., and McCoy, T.J. (2018) Acapulcoite-lodranite meteorites: Ultramafic asteroidal partial
454 melt residues. Chemie der Erde – Geochemistry, 78, 153–203.
455 Khisina, N.R., Wirth, R., and Abdrakhimov, A.M. (2019) Liquid immiscibility in regions of
456 localized shock-induced melting in the Elga meteorite. Geochemistry International, 57, 903–
457 911.
458 Kroll, H., Lueder, T., Schlenz, H., Kirfel, A., and Vad, T. (1997) The Fe^{2+}-Mg distribution in
459 orthopyroxene: a critical assessment of its potential as a geospeedometer. European Journal of
460 Mineralogy, 9, 705–733.
461 La Cruz, N.L., Qasim, D., Abbott-Lyon, H., Pirim, C., McKee, A.D., Orlando, T., Gull, M.,
462 Lindsay, D., and Pasek, M.A. (2016) The Evolution of the Surface of the Mineral Schreibersite
463 in Prebiotic Chemistry. Physical Chemistry Chemical Physics, 18, 20160−20167.
464 Li, C., Gao, H., Wan, W., Mueller, T. (2019) Mechanisms for hydrogen evolution on transition
465 metal phosphide catalysts and a comparison to Pt(111). Physical Chemistry Chemical Physics,
466 21, 24489–24498.

Li, S.J., Wang, S.J., Bao, H.M., Miao, B.K., Liu, S., Coulson, I.M., Li, X.Y., and Li, Y. (2011) The Antarctic achondrite, Grove Mountains 021663: An olivine-rich winonaite. Meteoritics & Planetary Science, 46, 1329–1344.

Macrae, C.F., Edgington, P.R., McCabe, P., Pidcock, E., Shields, G.P., Taylor, R., Towler, M., and van de Streek, J. (2006) Mercury: visualization and analysis of crystal structures. Journal of Applied Crystallography, 39, 453–457.

Moretzki, O., Morgenroth, W., Skala, R., Szymanski, A., Wendschuh, M., Geist, V. (2005) Determination of the metal ordering in meteoritic $(Fe,Ni)_3P$ crystals. Journal of Synchrotron Radiation, 12, 234–240.

Parker, E.T., Cleaves H.J., Bada, J.L., and Fernández, F.M. (2016) Quantitation of α-hydroxy acids in complex prebiotic mixtures via liquid chromatography/tandem mass spectrometry. Rapid Communications in Mass Spectrometry, 30, 2043–2051.

Pasek, M.A. (2008) Rethinking early Earth phosphorus geochemistry. Proceedings of the National Academy of Sciences, 105, 853–858.

Pasek, M.A., Dworkin, J.P., and Lauretta, D.S. (2007) A radical pathway for organic phosphorylation during schreibersite corrosion with implications for the origin of life. Geochimica et Cosmochimica Acta, 71, 1721–1736.

Pasek, M.A. (2020) Thermodynamics of Prebiotic Phosphorylation. Chemical Reviews, 120, 4690–4706.

Pech, H., Vasquez, M., Van Buren, J., Xu, L., Salmassi, T., Pasek, M.A., and Foster, K. (2011) Elucidating the redox cycle of environmental phosphorus using ion chromatography. Journal of Chromatographic Science, 49, 573–581.

Pirim, C., Pasek, M.A., Sokolov, D.A., Sidorov, A.N., Gann, R.D., and Orlando, T.M. (2014) Investigation of schreibersite and intrinsic oxidation products from Sikhote-Alin, Seymchan,

and Odessa meteorites and Fe_3P and Fe_2NiP synthetic surrogates. Geochimica et Cosmochimica Acta, 140, 259–274.

Rundqvist, S. (1962) X-ray investigations of the ternary system Fe–B–P. Acta Chemica Scandinavica, 16, 1–19.

Rundqvist, S., Hassler, E., and Lundvik, L. (1962) Refinement of the Ni_3P structure. Acta Chemica Scandinavica, 16, 242–243.

Scott, H.P., Huggins, S., Frank, M.R., Maglio, S.J., Martin, C.D., Meng, Y., Santillán, J., and Williams, Q. (2007) Equation of state and high-pressure stability of Fe_3P-schreibersite: Implications for phosphorus storage in planetary cores. Geophysical Research Letters, 34, L06302.

Sheldrick, G.M. (2015a) Crystal structure refinement with *SHELXL*. Acta Crystallographica, C71, 3–8.

Sheldrick, G.M. (2015b) *SHELXT* – integrated space-group and crystal structure determination. Acta Crystallographica, A71, 3–8.

Skála, R., and Císařová, I. (2005) Crystal structure of meteoritic schreibersites: determination of absolute structure. Physics and Chemistry of Minerals, 31, 721–732.

Skála, R., and Drábek, M. (2000) Variation of unit-cell dimensions of experimentally synthesized members of Fe_3P–Ni_3P solid solution. 31st Lunar and Planetary Science Conference, Houston, abstract #1564.

Skála, R., and Drábek, M. (2003) Nickelphosphide from the Vicenice octahedrite: Rietveld crystal structure refinement of a synthetic analogue. Mineralogical Magazine, 67, 783–792.

Smith, J.V., and Steele, I.M. (1976) Lunar mineralogy: a heavenly detective story. Part II. American Mineralogist, 61, 1059–1116.

Spriggs, P.H. (1970) An investigation of the variation of lattice parameters with composition along the tie-line Ni_3P-Fe_3P. Philosophical Magazine, 21, 897–901.

516 Warner, J.K., Cheetham, A.K., and Cox, D.E. (1995) Determination of the cation distribution in
517 $NiFe_2(PO_4)_2$ using resonant X-ray and neutron powder diffraction. Journal of Applied
518 Crystallography, 28, 494–502.
519 Wasson, J.T., and Choe, W.-H. (2009) The IIG iron meteorites: Probable formation in the IIAB
520 core. Geochimica et Cosmochimica Acta, 73, 4879–4890.
521 Wasson, J.T., and Wai, C.M. (1970) Composition of the metal, schreibersite and perryite of enstatite
522 achondrites and the origin of enstatite chondrites and achondrites. Geochimica et
523 Cosmochimica Acta, 34, 169–184.
524 Wexler, R.B., Martirez, J.M.P., and Rappe, A.M. (2017) Active Role of Phosphorus in the
525 Hydrogen Evolving Activity of Nickel Phosphide (0001) Surfaces. ACS Catalysis, 7, 7718–
526 7725.
527 Westrip, S.P. (2010) *publCIF*: Software for Editing, Validating and Formatting Crystallographic
528 Information Files. Journal of Applied Crystallography, 43, 920−925.
529 Zen, E. (1956) Validity of "Vegard's law". American Mineralogist, 41, 523–524.
530 Zolensky, M.E., Nakamura, K., Gounelle, M., Mikouchi, T., Kasama, T., Tachikawa, O., and Tonui,
531 E. (2002) Mineralogy of Tagish Lake: An ungrouped type 2 carbonaceous chondrite.
532 Meteoritics & Planetary Science, 37, 737–761.
533

534 **List of figure captions**

535 **Figure 1.** Coordination polyhedra in the crystal structure of schreibersite. (a) Phosphorus-centered
536 polyhedron [PM_9]. (b) Coordination cage of *M*1 site (CN 15). (c) Coordination cage of *M*2 (CN 14).
537 (d) Coordination cage of *M*3 (CN 13). Legend: yellow, P; brown, *M*1; blue, *M*2; green, *M*3. Thermal
538 displacement ellipsoids are drawn at 50% probability level. Created based on the data for
539 schreibersite from the Bischtübe octahedrite, using CCDC Mercury software (Macrae et al. 2006).
540

541 **Figure 2.** Terrestrial schreibersite. (a) Single-crystal grain of schreibersite surrounded by the thick
542 rims of polycrystalline barringerite, $(Fe_{1.98}Ni_{0.02})_{2.00}P$. Phosphides are embedded into the matrix of
543 hydrous Ca-Mg silicates. Reflected light. (b) The same grain, SEM BSE image. The worm-like
544 channels in schreibersite are filled with an unknown Na-Fe phosphate. Halamish Wadi, Hatrurim
545 Basin, Negev desert, Israel. Schr, schreibersite; Brr, barringerite; Tr, troilite.
546

547 **Figure 3.** Plots of Ni contents as determined by EMPA *vs.* Ni contents obtained by summation of X-
548 ray refined site populations (Table 1). The linear fits are marked by red lines. (a) Single-crystal data:
549 $R^2 = 0.97$; intercept –0.00(4) Ni *apfu*; slope 1.00(4). (b) Rietveld refinement results: $R^2 = 0.98$;
550 intercept of –0.03(1) Ni *apfu*; slope 1.00(3). The dashed lines trace the theoretical tie-line Fe_3P–
551 Ni_3P.
552

553 **Figure 4.** Dependencies of unit-cell parameters of natural schreibersite and synthetic $(Fe,Ni)_3P$ upon
554 total Ni content. (a) The *a* parameter follows a flat 2nd order polynomial curve ($R^2 = 0.995$). (b)
555 Unit-cell volume can also be fitted with a 2nd order polynomial ($R^2 = 0.993$). (c) Divergence in
556 behaviour of the *c* parameter of natural schreibersite and synthetic $(Fe,Ni)_3P$. (d) Divergence in the
557 *c*/*a* parameter ratio between natural schreibersite and synthetic $(Fe,Ni)_3P$. The errors (esd's) are

558 smaller than size of the symbols. Data for natural schreibersite (red circles, this work) were taken
559 from Table 2. Data for synthetic $(Fe,Ni)_3P$: Skála and Drábek (2000, 2003).
560
561 **Figure 5.** The site-specific match between Ni populations determined by single-crystal and Rietveld
562 refinements. Linear fit for the *M*2 site: $R^2 = 0.95$; intercept 0.002(7) Ni *apfu*; slope 1.06(5). Linear
563 fit for the *M*3 site: $R^2 = 0.99$, intercept 0.001(4) Ni *apfu*; slope 0.93(2).
564
565 **Figure 6.** Plots of Ni site population versus total Ni content in natural schreibersite (Table 3). (a)
566 2nd order polynomial fits for the entire range of compositions. (b) Linear regressions for $0.58 \leq$
567 [total Ni] ≤ 1.54 *apfu.* Single-crystal refinement results. The dashed lines trace a theoretical join
568 Fe_3P–Ni_3P.
569
570 **Figure 7.** Dependencies of *c*/*a* ratio of natural schreibersite on Ni site population (Table 3). Single-
571 crystal refinement results.
572
573 **Figure 8.** Examples of site-specific dependencies between bond length and Ni site population of
574 natural schreibersite. (a) The *M*2—$M2^{ix}$ bond showing the most considerable decrease in length
575 upon increase of Ni population. (b) The *M*3—$M3^{vii}$ bond showing the strongest opposite behavior.
576 (c) Very complex variations for *M*1—$M3^{ii}$ bond. (d) The *M*2—P bond is virtually insensitive to
577 variations in Ni content. Vertical scale is the same in all plots. Single-crystal refinement results.
578 Symmetry codes: (ii) y, –x, –z+1; (vii) –x+1/2, –y–1/2, z–1/2; (ix) y+1/2, –x+1/2, –z+3/2.
579

This is the peer-reviewed, final accepted version for American Mineralogist, published by the Mineralogical Society of America.
The published version is subject to change. Cite as Authors (Year) Title. American Mineralogist, in press.
DOI: https://doi.org/10.2138/am-2021-7766. http://www.minsocam.org/

Tables

Table 1. Total Ni contents in schreibersite as determined by three methods [a]

Source [b]	Classification [c]	EMPA	Single-crystal [d]	Rietveld [d]
Hatrurim Basin (Htr)	Terrestrial	0.03(1)	n.d. [e]	n.d. [e]
Zacatecas (1792) (Zct)	Iron-ungr	0.40(1)	0.35(2)	0.31(1)
São Julião de Moreira (SJM)	IIB (Ogg)	0.50(1)	0.54(3)	0.58(1)
Madoc (Mad)	IIIAB (Om)	0.58(1)	0.59(2)	0.62(1)
Bischtübe (Bst)	IAB-sLL (Og)	0.58(1)	0.58(3)	0.57(1)
Toluca (Tol)	IAB-sLL (Og)	0.62(1)	0.64(3)	0.68(1)
Glorieta Mountain (GM)	PMG-an	0.64(1)	0.61(3)	0.70(1)
Augustinovka (Aug)	IIIAB (Om)	0.72(1)	0.79(2)	0.59(1)
Mont Dieu (MD)	IIE (Om)	0.92(2)	0.89(4)	0.83(1)
Lazarev (Lzr)	Iron-ungr (Pal?)	0.99(2)	0.96(4)	0.89(1)
Krasnojarsk (Krs)	PMG-an	1.00(2)	0.96(3)	1.08(1)
Seymchan (Sey)	PMG	1.00(2)	1.08(3)	1.07(1)
Brenham (Brh)	PMG-an	1.01(2)	1.01(4)	1.02(1)
Cranbourne (Crn1)	IAB-MG (Og)	1.03(2)	1.05(2)	1.00(1)
Magura (Mgr)	IAB-MG (Og)	1.08(2)	1.03(6)	0.84(1)
Canyon Diablo (CD1)	IAB-MG (Og)	1.13(2)	1.19(3)	1.07(1)
Cosby's Creek (Csb)	IAB-MG (Og)	1.13(2)	1.05(5)	1.15(1)
Petropavlovsk (Ptr)	Iron-ungr (Om)	1.13(2)	1.05(4)	0.86(1)
Springwater (Spr)	PMG	1.14(2)	1.11(4)	1.22(1)
Finmarken (Fnm2)	PMG	1.25(2)	1.17(4)	1.13(1)
Canyon Diablo (CD2)	IAB-MG (Og)	1.28(3)	1.24(2)	1.23(1)
Finmarken (Fnm3)	PMG	1.48(3)	1.59(3)	1.62(1)
Cranbourne (Crn2)	IAB-MG (Og)	1.54(3)	1.55(3)	1.60(3)

[a] Calculated on 4 atoms per formula unit; ordered by Ni content (ascending). [b] Meteorites, except for the mineral from the Hatrurim Basin. Sample codes are given in parentheses. [c] Meteorite classification according to Buchwald (1975) and Grady (2000). [d] Sums of Ni site populations obtained from X-ray structure refinements. [e] Not determined.

This is the peer-reviewed, final accepted version for American Mineralogist, published by the Mineralogical Society of America.
The published version is subject to change. Cite as Authors (Year) Title. American Mineralogist, in press.
DOI: https://doi.org/10.2138/am-2021-7766. http://www.minsocam.org/

590

591 **Table 2.** Absolute structure and unit-cell parameters of schreibersite [a]

Code	Flack x [b]	a (Å)	c (Å)	V (Å^3)	c/a
Htr	0.07(3)	9.1092	4.4621	370.25	0.4899
Zct	0.96(2)	9.0852	4.4661	368.64	0.4916
SJM	0.06(2)	9.0782	4.4655	368.02	0.4919
Mad	0.98(1)	9.0749	4.4654	367.74	0.4921
Bst	0.04(2)	9.0732	4.4651	367.58	0.4921
Tol	0.03(1)	9.0720	4.4651	367.48	0.4922
GM	0.03(3)	9.0698	4.4647	367.27	0.4923
Aug	0.39(2)	9.0683	4.4660	367.26	0.4925
MD	0.38(3)	9.0571	4.4660	366.35	0.4931
Lzr	0.97(1)	9.0532	4.4656	366.00	0.4933
Krs	0.04(1)	9.0487	4.4646	365.56	0.4934
Sey	0.97(2)	9.0509	4.4647	365.74	0.4933
Brh	0.03(1)	9.0495	4.4642	365.59	0.4933
Crn1	0.03(2)	9.0471	4.4647	365.44	0.4935
Mgr	0.03(2)	9.0s470	4.4644	365.40	0.4935
CD1	0.97(2)	9.0409	4.4638	364.86	0.4937
Csb	0.92(3)	9.0435	4.4649	365.16	0.4937
Ptr	0.03(2)	9.0424	4.4642	365.02	0.4937
Spr	0.96(1)	9.0426	4.4641	365.02	0.4937
Fnm2	0.06(3)	9.0416	4.4646	364.98	0.4938
CD2	0.01(1)	9.0363	4.4644	364.54	0.4941
Fnm3	0.54(3)	9.0279	4.4637	363.80	0.4944
Crn2	0.01(1)	9.0242	4.4620	363.37	0.4944

592
593 [a] Estimated standard deviations: a 5×10^{-4} Å; c 3×10^{-4} Å; V 0.05 Å^3. [b] Absolute
594 structure parameter determined from the single-crystal data (Flack and Bernardinelli
595 1999), relative to standard setting by Doenitz (1970).
596
597

This is the peer-reviewed, final accepted version for American Mineralogist, published by the Mineralogical Society of America.
The published version is subject to change. Cite as Authors (Year) Title. American Mineralogist, in press.
DOI: https://doi.org/10.2138/am-2021-7766. http://www.minsocam.org/

598
599 **Table 3.** Refined Ni populations at the metal sites of schreibersite
600

Code	Single-crystal data		Rietveld refinement	
	***M*2**	***M*3**	***M*2**	***M*3**
Htr	0	0	0	0
Zct	0.08(2)	0.27(1)	0.11(1)	0.20(1)
SJM	0.09(2)	0.44(2)	0.15(1)	0.43(1)
Mad	0.13(2)	0.46(2)	0.21(1)	0.41(1)
Bst	0.11(2)	0.47(2)	0.14(1)	0.43(1)
Tol	0.10(2)	0.54(2)	0.17(1)	0.51(1)
GM	0.11(2)	0.50(2)	0.19(1)	0.51(1)
Aug	0.21(2)	0.58(1)	0.12(1)	0.47(1)
MD	0.22(3)	0.67(2)	0.23(1)	0.60(1)
Lzr	0.24(3)	0.72(2)	0.28(1)	0.61(1)
Krs	0.26(2)	0.70(2)	0.40(1)	0.68(1)
Sey	0.33(2)	0.75(2)	0.33(1)	0.74(1)
Brh	0.26(3)	0.75(2)	0.34(1)	0.68(1)
Crn1	0.33(2)	0.72(1)	0.31(1)	0.69(1)
Mgr	0.31(5)	0.72(4)	0.26(1)	0.58(1)
CD1	0.39(2)	0.80(2)	0.34(1)	0.73(1)
Csb	0.32(4)	0.73(3)	0.42(1)	0.73(1)
Ptr	0.38(3)	0.67(3)	0.27(1)	0.59(1)
Spr	0.32(3)	0.79(2)	0.42(1)	0.80(1)
Fnm2	0.37(3)	0.80(2)	0.42(1)	0.71(1)
CD2	0.41(2)	0.83(1)	0.44(1)	0.79(1)
Fnm3	0.59(3)	1	0.62(1)	1
Crn2 [a]	0.55(3)	1	0.67(1)	0.88(2)

601
602 [a] Besides, Rietveld refinement gave 0.05(1) Ni in the *M*1 site.

603

This is the peer-reviewed, final accepted version for American Mineralogist, published by the Mineralogical Society of America.
The published version is subject to change. Cite as Authors (Year) Title. American Mineralogist, in press.
DOI: https://doi.org/10.2138/am-2021-7766. http://www.minsocam.org/

Figures

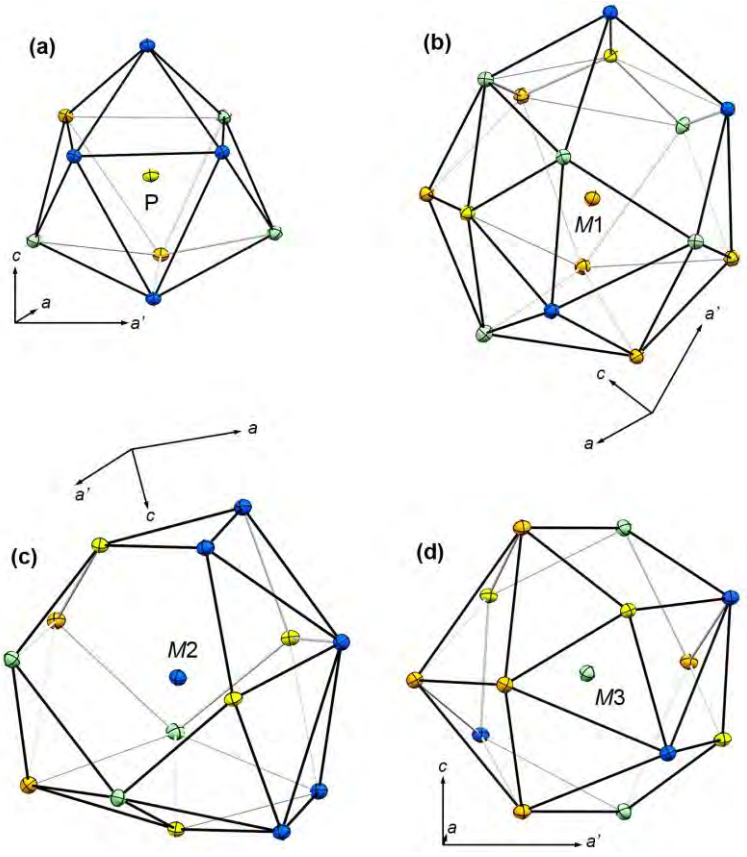

Figure 1

This is the peer-reviewed, final accepted version for American Mineralogist, published by the Mineralogical Society of America.
The published version is subject to change. Cite as Authors (Year) Title. American Mineralogist, in press.
DOI: https://doi.org/10.2138/am-2021-7766. http://www.minsocam.org/

618

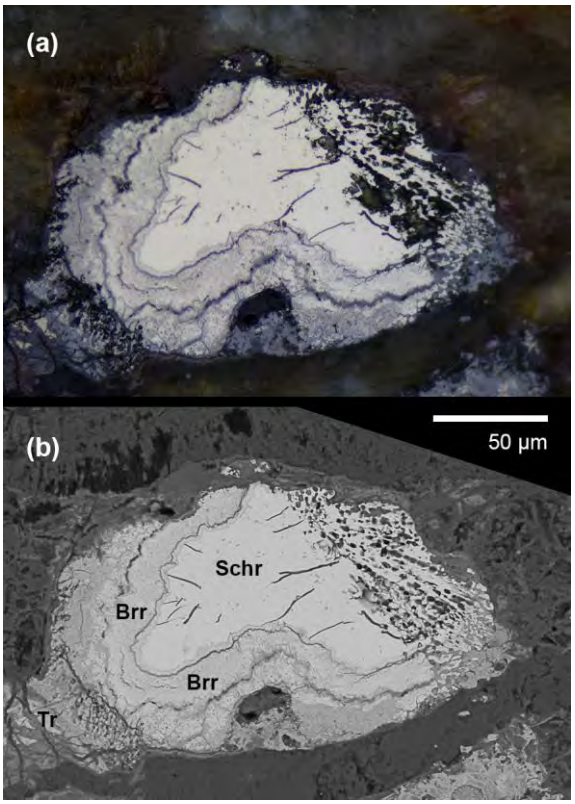

619

620 **Figure 2**

621

622

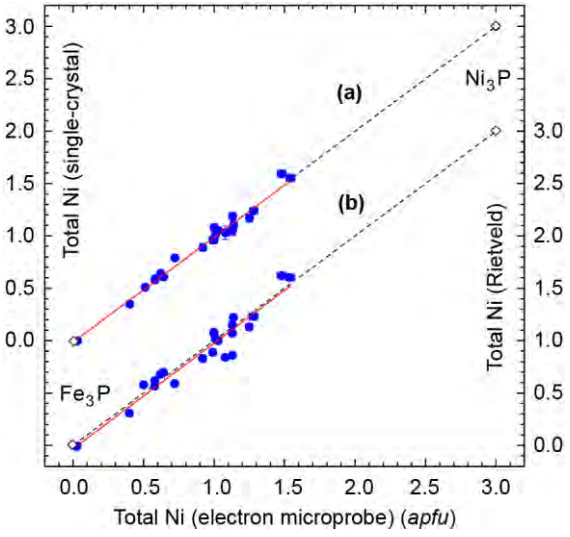

623

624 **Figure 3**

625

This is the peer-reviewed, final accepted version for American Mineralogist, published by the Mineralogical Society of America.
The published version is subject to change. Cite as Authors (Year) Title. American Mineralogist, in press.
DOI: https://doi.org/10.2138/am-2021-7766. http://www.minsocam.org/

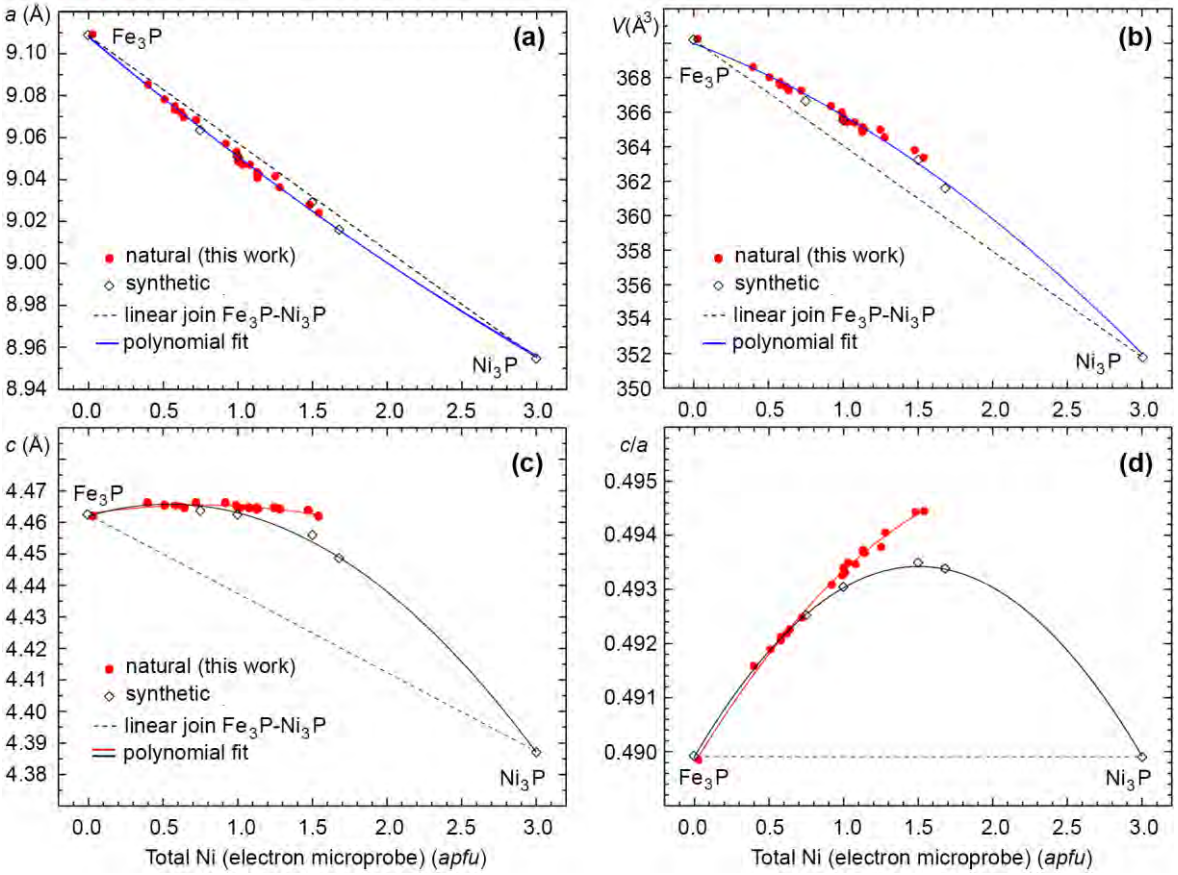

Figure 4

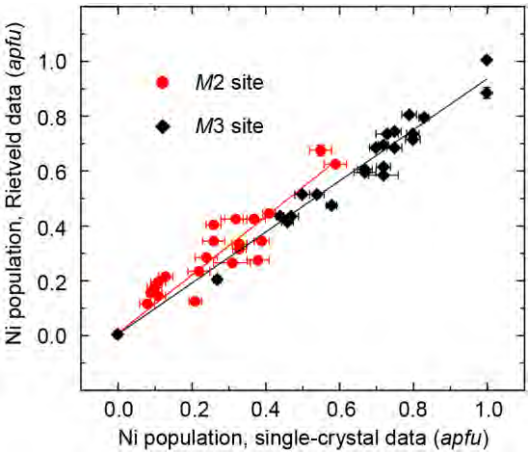

Figure 5

This is the peer-reviewed, final accepted version for American Mineralogist, published by the Mineralogical Society of America.
The published version is subject to change. Cite as Authors (Year) Title. American Mineralogist, in press.
DOI: https://doi.org/10.2138/am-2021-7766. http://www.minsocam.org/

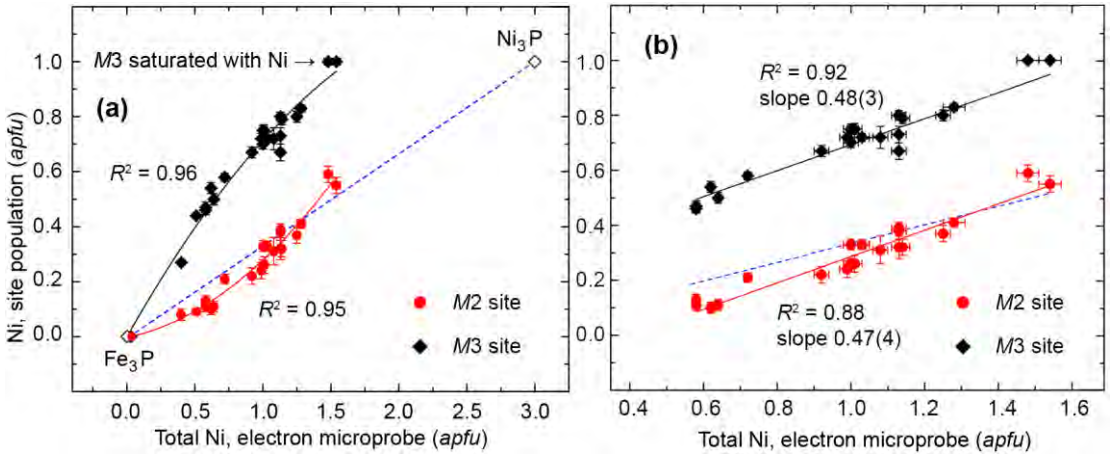

Figure 6

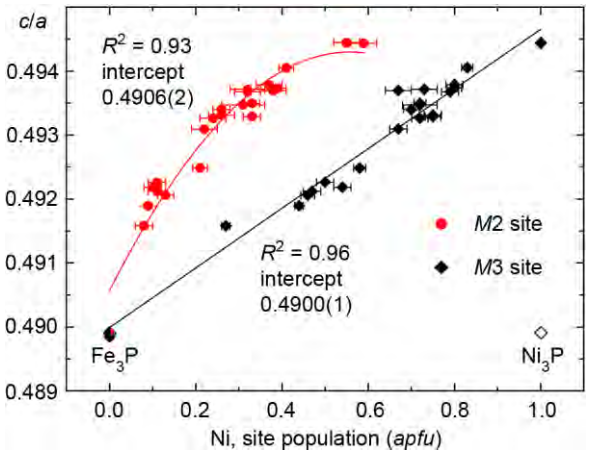

Figure 7

This is the peer-reviewed, final accepted version for American Mineralogist, published by the Mineralogical Society of America.
The published version is subject to change. Cite as Authors (Year) Title. American Mineralogist, in press.
DOI: https://doi.org/10.2138/am-2021-7766. http://www.minsocam.org/

645

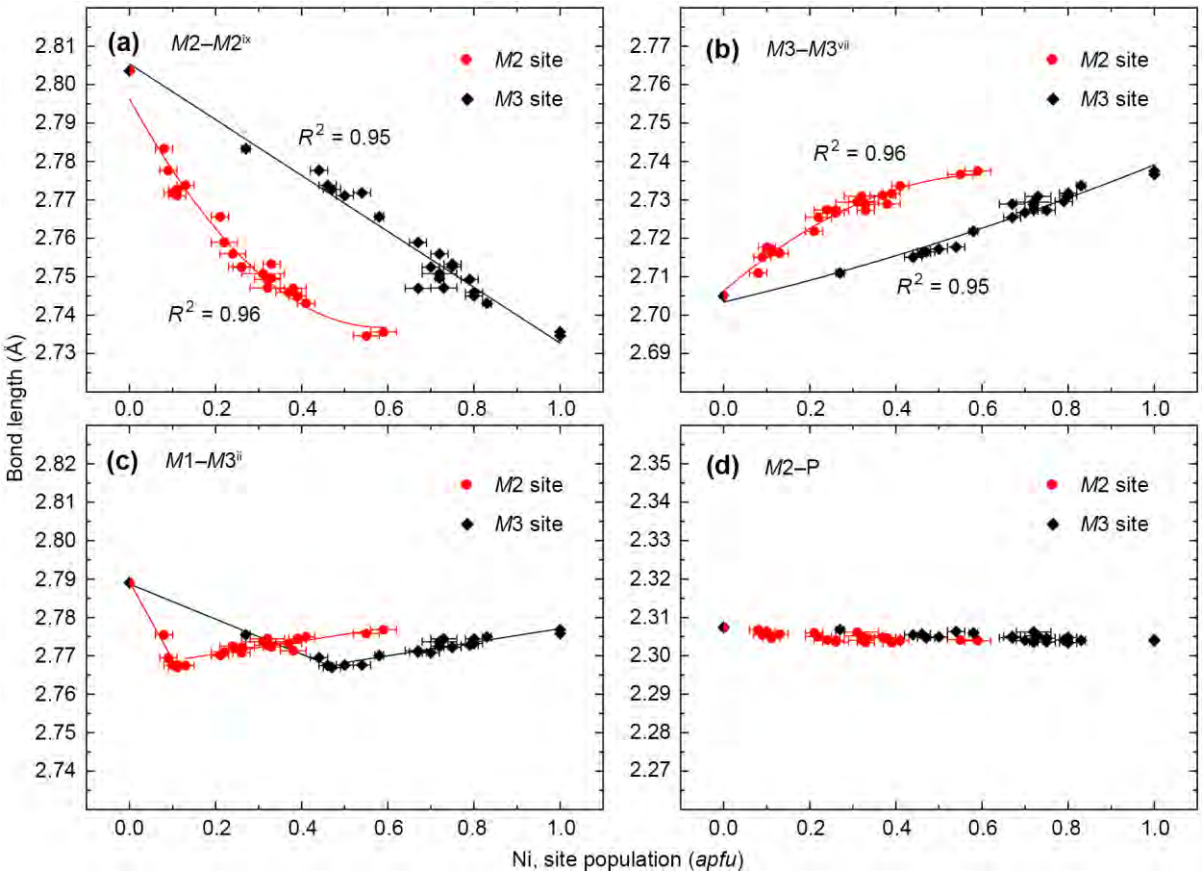

646

647 **Figure 8**